Electromyography-driven model-based estimation of ankle torque and stiffness during dynamic joint rotations in perturbed and unperturbed conditions

Christopher P. Cop[a,*], Alfred C. Schouten[a,b], Bart Koopman[a], Massimo Sartori[a]

[a] *Department of Biomechanical Engineering, University of Twente, Enschede, The Netherlands*

[b] *Department of Biomechanical Engineering, Delft University of Technology, Delft, The Netherlands*

Keywords: joint stiffness, musculoskeletal modeling, calibration, electromyography

Word count: 3146

*Corresponding author
Email address: c.p.cop@utwente.nl, +31534898411 (Christopher P. Cop)

Abstract

The simultaneous modulation of joint torque and stiffness enables humans to perform large repertoires of movements, while adapting to external mechanical demands in a versatile way. Multi-muscle force control is key for joint torque and stiffness modulation. However, the inability to directly measure muscle force in the intact moving human prevents understanding how muscle force causally links to joint torque and stiffness during movement. Joint stiffness is predominantly estimated via joint perturbation-based experiments in combination with system identification techniques. However, these techniques provide joint-level stiffness estimations with no causal link to the underlying muscle forces. Moreover, the need for joint perturbations limits the generalisability and applicability to study natural movements. Here, we present an electromyography (EMG)-driven musculoskeletal modeling framework that can be calibrated to match reference joint torque and stiffness profiles simultaneously. EMG-driven models calibrated on < 2 s of reference torque and stiffness data could blindly estimate reference profiles across 100 s of data not used for calibration. Torque-and-stiffness calibrated models reduced the space of feasible muscle-tendon unit parameters with respect to torque-only calibrated models, thereby addressing the model redundancy problem. Results also showed the ability of the proposed framework to estimate joint stiffness in unperturbed conditions, while capturing differences against stiffness profiles derived during perturbed conditions. The proposed framework may provide new ways for studying causal relationships between muscle force and joint torque and stiffness during natural movements in interaction with the environment, with broad implications across biomechanics, rehabilitation and robotics.

Keywords: joint stiffness, musculoskeletal modeling, calibration, electromyography

1. Introduction

Human movement results from the interaction between the neuromusculoskeletal system and the environment (Winter, 2009). The coordinated activity of all muscles spanning a joint largely defines net joint torque and joint stiffness (Cop et al., 2021), thereby enabling versatile navigation and adaptation to external mechanical demands (Valero-Cuevas, 2016). The ability to determine the muscle force profiles underlying a given movement is crucial to understand how joint torque and stiffness are modulated to enable large repertoires of movements. However, it is currently not possible to directly measure muscle force in the intact moving human *in vivo* (Herzog, 2017).

Electromyography (EMG)-driven musculoskeletal models (or EMG-driven models) are valuable computational tools to study movement's underlying musculoskeletal forces (Lloyd and Besier, 2003). In this context, muscle-tendon units (MTUs) are predominantly modeled using Hill-type muscle formulations, based on parameters that vary non-linearly across individuals. However, for the same person, and for the same combination of joint angle and torque profiles, different model parameters could potentially result in different muscle force and joint stiffness solutions (Cop et al., 2021). Therefore, robust identification of MTU parameters on a subject-specific basis is necessary to understand how muscles contribute to modulate joint stiffness during movement.

EMG-driven model parameters are commonly identified to best fit experimental joint torques (Falisse et al., 2016). However, it is unclear to what extent Hill-type muscle models with torque-only-identified parameters would enable estimation of joint stiffness (Perreault et al., 2003; Hu et al., 2011). Human joint stiffness is predominantly studied via system identification methods, which require the mechanical perturbation of biological joints (Kearney and Hunter, 1990). However, the required joint perturbation inherently alters normative neuromuscular function and limits the repertoire of movements, as well as the range of human populations, that can be studied in the first place (Klomp et al., 2013). Moreover, joint-perturbation-based system identification methods provide estimations of joint-level stiffness with no direct link to the underlying muscle forces.

First, we propose a new EMG-driven model that can be calibrated at the joint torque and stiffness levels simultaneously during dynamic ankle joint rotations. We hypothesize this will improve joint stiffness estimation with respect to torque-only calibrated models. Moreover, we hypothesise torque-and-stiffness calibrated models reduce the MTU parameter solution space with respect to torque-only calibrated models, thereby leading to realistic MTU force solutions, i.e., explaining joint stiffness and torque simultaneously. Second, we assess the ability of the proposed modeling framework to estimate joint stiffness in unperturbed conditions, while capturing differences against stiffness profiles derived during conventional perturbed conditions.

This study provides a framework to study how muscle force results in torque and stiffness modulation during dynamic movements in perturbed and unperturbed conditions. Removing the need for joint perturbation would enable, for

the first time, the ability to study the neural control of joint stiffness in natural, unaffected biological systems, while facilitating translation to clinical settings, where joint-perturbation requirements cannot always be met (Sartori et al., 2015).

2. Methods

2.1. Subjects

Five healthy volunteers (age range: 23–30 years, 1 woman) with no self-reported history of neurological or ankle impairments participated in this study. The Natural Sciences and Engineering Sciences Ethics Committee of the University of Twente approved the experimental procedures (reference number: RP 2018-59) and all subjects provided written informed consent. The experiments complied with the Declaration of Helsinki.

2.2. Protocol

The "Achilles" Rehabilitation Device (MOOG, Nieuw-Vennep, The Netherlands), a single axis dynamometer, was used to perturb and measure subjects' right ankle joint angle and torque at 2048 Hz. The right ankle's axis of rotation in the sagittal plane was visually aligned to the actuator's axis of rotation before the start of the experiment. The chair was adjusted to allow for a knee flexion angle of 45°. Subjects were instructed to follow a sinusoidal ankle angle target (amplitude: 0.15 rad, frequency: 0.6 Hz) displayed on a monitor, while small pseudo-random angular perturbations (amplitude: 0.03 rad, switching time: 0.15 s) were applied. The dynamometer controller was set to render a virtual environment: inertia: 1 kg·m^2, damping: 2.5 N·m·s/rad, stiffness: 60 N·m/rad. Additionally, four subjects also performed the same tracking task, i.e., sinusoidal ankle angle target (amplitude: 0.15 rad, frequency: 0.6 Hz), without being applied any angular perturbations by the dynamometer, i.e., unperturbed trial.

EMGs were recorded (2048 Hz) using a 32-channel amplifier (Porti, TMSi, Oldenzaal, The Netherlands) and disc-shaped Ag / AgCl electrodes (inter-electrode distance: 24 mm) in a bipolar configuration. Electrodes were placed following SENIAM guidelines (Hermens et al., 2000) on tibialis anterior, soleus, gastrocnemius medialis, gastrocnemius lateralis, and peroneus longus. Three maximum voluntary contraction (MVC) trials of approximately 5 s per muscle group were performed at the start of the experiment to normalize the EMGs.

2.3. Data processing

Data processing was performed using MATLAB R2021a (The Mathworks Inc., Natick, MA, USA). EMG signals were band-pass filtered using a zero-lag second-order Butterworth filter (cutoff frequencies: [20 300] Hz), full-wave rectified, and low-pass filtered (cutoff frequency: 3 Hz) using a zero-lag second-order Butterworth filter. The resulting envelopes were normalized and resampled at 1024 Hz. In the remainder of the manuscript these normalized EMG envelopes

will be referred to as "muscle excitations". Measured joint torques and joint angle were low-pass filtered using a zero-lag fourth order Butterworth filter (cutoff frequency: 80 Hz) and resampled at 128 Hz. Processed joint torques and angles will be referred to as reference joint torque and angle profiles.

Reference joint stiffness profiles were obtained using the Short Data Segments system identification algorithm (Ludvig and Perreault, 2012; Esteban et al., 2019). This method uses ensembles of input, i.e., joint angular displacement due to perturbation, and output, i.e., measured response torque, data across an ensemble of realizations to estimate joint stiffness at each time point (van de Ruit et al., 2021). Reference joint stiffness profiles were filtered using a moving average window of 20 samples.

2.4. EMG-driven musculoskeletal modeling

This work extends the Calibrated EMG-Informed Neuromusculoskeletal Modelling Toolbox (CEINMS) we previously developed (Pizzolato et al., 2015; Durandau et al., 2017). We introduce a new algorithm to calibrate EMG-driven model parameters both at the stiffness and torque levels simultaneously. Moreover, we extend previous Hill-type muscle model formulations (Sartori et al., 2015) to allow for stiffness estimation accounting for MTUs' pennation angle. For an extensive description of the standard EMG-driven modeling formulation via Hill-type muscle models, the reader is referred to (Lloyd and Besier, 2003; Sartori et al., 2015). The EMG-driven modeling pipeline (Fig. 1) is outlined below.

Activation dynamics:. Muscle excitations are mapped into MTU activations (a):

$$a = \frac{e^{Au} - 1}{e^{A} - 1} \tag{1}$$

where u is the experimental muscle excitation, and A $\in$ (-3, 0) is the shape factor.

MTU kinematics:. Joint angles are mapped into MTU length and moment arms using a set of multi-dimensional B-splines (Sartori et al., 2012).

MTU dynamics:. MTU force, F^{mtu}, is computed as a function of MTU length, velocity, activation, and pennation angle:

$$F^{mtu} = F^{max}\big(a f_a(\tilde{l}^m) f_v(\tilde{v}^m) + f_p(\tilde{l}^m) + \bar{v}^m d\big)\cos\phi \tag{2}$$

where F^{max} is the muscle's maximum isometric force, $f_a(\tilde{l}^m)$, $f_v(\tilde{v}^m)$, and $f_p(\tilde{l}^m)$ are generic dimensionless active force-length, force-velocity, and passive force-length relationships, respectively, $\tilde{l}^m$ and $\tilde{v}^m$ are the muscle fiber's normalized length and velocity, respectively, $d = 0.1$ is a damping factor to avoid model singularities when muscles are inactive (Millard et al., 2013), and ϕ is the muscle fiber's pennation angle.

MTU stiffness, K^{mtu}, is computed as the series arrangement of the equivalent muscle fiber's stiffness in the tendon's line of action, K^m_{eq}, and the tendon's stiffness, K^t, (Cop et al., 2021):

$$K^{mtu} = \left(K^{m\,-1}_{eq} + K^{t\,-1}\right)^{-1} \tag{3}$$

where, based on the work of (Jenkins and Bryant, 2020), K^m_{eq} is computed in a generalised way, i.e., considering pennation angle, as:

$$\begin{aligned} K^m_{eq} &= \frac{\partial F^m_{eq}(a, \tilde{l}^m, \tilde{v}^m, \phi)}{\partial l^m_{eq}} \\ &= \frac{\partial F^m(a, \tilde{l}^m, \tilde{v}^m)}{\partial l^m} \cos^2\phi + \frac{F^m(a, \tilde{l}^m, \tilde{v}^m)}{l^m} \sin^2\phi \end{aligned} \tag{4}$$

where F^m_{eq} and l^m_{eq} are the force and length, respectively, of the muscle fiber along the direction of the tendon's line of action, F^m and l^m are the force and length, respectively, of the muscle fiber along its axis. K^t is computed as:

$$K^t = \frac{dF^t(\epsilon)}{d\epsilon} \tag{5}$$

where $F^t(\epsilon)$ is the non-linear tendon force as a function of tendon strain ϵ ($\epsilon = l^t/l^t_s - 1$, where l^t is the tendon length and l^t_s is the tendon slack length).

Joint torque and stiffness computation:. MTU forces are projected into the joint level to obtain joint torque τ:

$$\tau = \sum_{i=1}^{\#mtu} F^{mtu}_i r_i \tag{6}$$

where r_i is the moment arm of the ith MTU spanning the joint.

The net joint stiffness, K^J, is computed as:

$$K^J = \sum_{i=1}^{\#mtu} (K^{mtu}_i r^2_i - \frac{\partial r_i}{\partial \theta} \cdot F^{mtu}_i) \tag{7}$$

where K^{mtu}_i represents the stiffness of the ith MTU spanning the joint, and θ is the joint angle.

Model calibration at the joint torque and stiffness levels simultaneously:. The optimal fiber length, tendon slack length, maximum isometric force, and shape factor of each MTU included in the model are calibrated using a simulated annealing optimization routine (Goffe et al., 1994) that minimizes the following multi-term objective function:

$$\begin{aligned} F_{obj} = \frac{1}{N_t} \sum_{t}^{\#Trials} \frac{1}{N_d} \sum_{d}^{\#DOFs} \frac{1}{N_s} \sum_{s}^{\#Samples} \alpha \left(\frac{(\overline{\tau_{t,d,s}} - \tau_{t,d,s})^2}{Var(\overline{\tau_{t,d}})} \right) + \\ + \beta \left(\frac{(\overline{K_{t,d,s}} - K_{t,d,s})^2}{Var(\overline{K_{t,d}})} \right) + p_s \end{aligned} \tag{8}$$

where N_t, N_d, and N_s are the number of trials, DOFs, and samples, respectively, used to calibrate the model, α and β are weights to the contributions to the objective function of the estimated torques and stiffness, respectively, $\overline{\tau_{t,d}}$ and $\overline{K_{t,d}}$ are reference joint torque and stiffness values, respectively, $\tau_{t,d}$ and $K_{t,d}$ are modeled joint torque and stiffness values, respectively, and p_s is a newly introduced penalty factor that penalizes non-physiological normalized muscle lengths ($\tilde{l}^m < 0.5$ or $\tilde{l}^m > 1.5$) and negative tendon strains ($l^t < l^t_s$).

2.5. Data analysis

Simulations were performed using OpenSim 4.2 (Delp et al., 2007; Seth et al., 2018), and the real-time version of CEINMS (Durandau et al., 2017).

For each subject, the generic gait2392 OpenSim model (Delp et al., 1990) was linearly scaled to match their anthropometry. A previously proposed optimization-based method (Modenese et al., 2016) was used to identify initial values for MTU's optimal fiber length and tendon slack length in such a way that their operating range was preserved, with respect to the generic gait2392 OpenSim model, after the linear scaling. Lastly, optimal fiber length, tendon slack length, maximal isometric force and shape factor were further adjusted using our proposed calibration procedure (Section 2.4) to best fit experimental joint torque and stiffness simultaneously (Fig. 1).

For each calibration, only one cycle of the tracking task (≈1.6 s of data) was used. For each subject, calibrations using 35 combinations of α and β (α and β values going from 0 to 1 with a step length of 0.2) were executed. Due to the stochastic component of the simulated annealing algorithm (Goffe et al., 1994), the calibrations using each combination of α and β were repeated five times to assure convergence to the objective function's global optimum (8). Two calibrated EMG-driven models per subject were selected: the best fit to the torque and stiffness simultaneously, i.e. "Torque and stiffness", and the calibration with $\alpha = 1$ and $\beta = 0$ that best matched the experimental joint torque, i.e. the traditional "Torque only" calibration.

The two selected calibrated EMG-driven models were then used to estimate joint torques and stiffness using 100 s (approximately 60 cycles) of new, unseen EMGs and joint angles that were not employed for calibration.

2.6. Validation procedures

The results of the simulations and the input data were segmented into cycles and time-normalized between 0 and 100% of the cycle. Three tests were performed.

First test:. Validation of the estimated joint torque and stiffness against reference data for the two calibrated EMG-driven models. The root-mean-squared error normalized by the root-mean sum (nRMSE) and the squared Pearson correlation coefficient (r^2) were computed.

Second test:. Assessing parameter solution space dimensionality differences between validating only at the torque level and validating at the torque and stiffness levels simultaneously. We computed, for the best fitting calibration of each of the 35 combinations of α and β, the fitting error at the joint torque level ($\left(\frac{(\overline{\tau}-\tau)^2}{Var(\overline{\tau})}\right)$) and the total torque + stiffness fitting error ($\left(\frac{(\overline{\tau}-\tau)^2}{Var(\overline{\tau})}\right)+\left(\frac{(\overline{K}-K)^2}{Var(\overline{K})}\right)$). We compared how many calibrated EMG-driven models obtained acceptable torque fit (torque error $\leq \min(Error_{\tau}) + 0.1$) and how many calibrated EMG-driven models obtained acceptable torque and stiffness fit (total torque + stiffness fitting error $\leq \min(Error_{\tau+K}) + 0.1$). Additionally, we checked that those calibrated EMG-driven models that obtained a similar torque error underlay different sets of parameters.

Third test:. Estimation of joint stiffness via EMG-driven modeling using data from an unperturbed trial and comparison to the results from perturbed counterpart. Using the "Torque and stiffness" calibrated EMG-driven model, we qualitatively compared measured joint torques and joint angles from perturbed and unperturbed data. The corresponding joint stiffness estimations were compared via root-mean-squared error (RMSE) and r^2 metrics, and a two-sample t-test ($\alpha = 0.05$) was performed to identify regions in which the joint stiffness estimations were different with statistical significance.

3. Results

3.1. First test

Fig 2 shows the averaged joint torque and stiffness profiles per subject, derived from EMG-driven models calibrated via the "Torque only" and "Torque and stiffness" conditions. The joint torque and joint stiffness nRMSEs across all subjects for the "Torque only" model ranged between 0.17 and 0.78 (median: 0.38) and 0.19 and 0.92 (median: 0.64), respectively. The joint torque and joint stiffness nRMSEs across all subjects for the "Torque and stiffness" model ranged between 0.23 and 0.94 (median: 0.48) and 0.14 and 0.64 (median: 0.32), respectively. The joint torque and joint stiffness r^2 values across all subjects for the "Torque only" EMG-driven model ranged between 0.56 and 0.97 (median: 0.88) and 3.5×10^{-5} and 0.92 (median: 0.11), respectively. The joint torque and joint stiffness r^2 values across all subjects for the "Torque and stiffness" EMG-driven model ranged between 0.53 and 0.96 (median: 0.83) and 3.4×10^{-4} and 0.93 (median: 0.49), respectively. Table 1 summarizes nRMSE and r^2 values for each subject. Fig. 3 depicts the distribution of nRMSE and r^2 values across all subjects and cycles.

3.2. Second test

For every subject, the set of α and β combinations that yielded a similar torque error (i.e., red circles in Fig. 4) always had greater dimensionality than the set of α and β combinations that yielded a similar total torque + stiffness

Table 1: Normalized root-mean-squared error (nRMSE) and squared Pearson correlation coefficient (r^2) values between estimated and reference joint torques and stiffness for each subject. Results expressed as median (interquartile range). Results of the "Torque only" calibrated EMG-driven model in gray font, and results of the "Torque and stiffness" calibrated EMG-driven model in black font.

Subject	nRMSE		r^2	
	Torque	Stiffness	Torque	Stiffness
1	0.37 (0.08)	0.50 (0.10)	0.89 (0.05)	0.69 (0.26)
	0.41 (0.10)	0.23 (0.08)	0.88 (0.05)	0.83 (0.10)
2	0.36 (0.06)	0.63 (0.09)	0.88 (0.03)	0.01 (0.04)
	0.43 (0.08)	0.46 (0.08)	0.82 (0.07)	0.05 (0.09)
3	0.44 (0.11)	0.39 (0.16)	0.85 (0.09)	0.54 (0.41)
	0.73 (0.16)	0.28 (0.10)	0.84 (0.10)	0.59 (0.30)
4	0.32 (0.08)	0.71 (0.06)	0.92 (0.03)	0.04 (0.09)
	0.52 (0.14)	0.21 (0.06)	0.80 (0.09)	0.52 (0.21)
5	0.39 (0.06)	0.77 (0.07)	0.87 (0.05)	0.05 (0.13)
	0.44 (0.06)	0.44 (0.10)	0.85 (0.06)	0.46 (0.21)

error (i.e., blue circles in Fig. 4). Results also showed that all the α and β combinations that yielded a similar torque error underlay different parameter values and therefore represented actual different model instances (Fig. 5)). Across all subjects and modeled MTUs, the median interquartile ranges of the calibrated values of optimal fiber length, tendon slack length, strength coefficient, and shape factor spanned 47%, 42%, 38%, and 50%, respectively, of the permitted values.

From all α and β combinations with similar torque errors, only a subset of combinations minimized the total torque + stiffness fitting error ($\leq \min(Error_{\tau+K}) + 0.1$), i.e. blue circles in Fig. 4. For subject 1, 24 combinations of α and β resulted in similar torque fits, but only 8 minimized both torque and stiffness simultaneously. For subject 2, 28 combinations of α and β resulted in similar torque fit, but only 1 minimized both torque and stiffness simultaneously. For subject 3, 26 combinations of α and β resulted in similar torque fit, but only 2 minimized both torque and stiffness simultaneously. For subject 4, 30 combinations of α and β resulted in similar torque fit, but only 1 minimized both torque and stiffness simultaneously. For subject 5, 28 combinations of α and β resulted in similar torque fit, but only 6 minimized both torque and stiffness simultaneously.

3.3. Third test

Fig. 6 shows, for each subject individually and for the average across all subjects, average joint torque, angle, and stiffness profiles for both the perturbed and unperturbed data. The joint stiffness RMSEs across all subjects between perturbed and unperturbed data ranged between 2.4×10^{-3} N·m/rad and 3.41

N·m/rad (median: 0.77 N·m/rad). The joint stiffness r^2 values across all subjects between perturbed and unperturbed data ranged between 5.4×10^{-4} and 0.97 (median: 0.67). All subjects, in addition to the average across subjects, showed statistically different joint stiffness profiles in portions of the task cycle: 27%, 69%, 78%, 39% of the whole cycle for subjects 1 – 4, respectively, and 35% of the whole cycle for the average across all subjects.

4. Discussion

We proposed an EMG-driven model-based stiffness estimation methodology, which we validated against the joint perturbation-based Short Data Segments system identification method using data from the same subject population and movement. Differently from joint perturbation-based methods, our approach provides a direct link between joint stiffness and the underlying EMG and muscle force profiles, something crucial to study causalities between neural, muscular and articular dynamics.

Previous research highlighted the predominant contribution of short-range stiffness to the model-based estimation of arm end-point stiffness during isometric contractions only (Hu et al., 2011). However, it was never investigated to what extent EMG-driven Hill-type muscle models could estimate reference joint stiffness profiles during dynamic tasks, during which short-range stiffness components would play a less predominant role (Cop et al., 2021).

The first test showed that EMG-driven models calibrated under the "Torque only" condition displayed only minimal improvements at estimating reference joint torque profiles, compared to models calibrated under the "Torque and stiffness" condition (median nRMSE reduced by 0.1; median r^2 increased by 0.05). However, EMG-driven models calibrated under the "Torque and stiffness" condition outperformed the "Torque only" models at estimating reference joint stiffness profiles (median nRMSE reduced by 0.32; median r^2 increased by 0.38, Figs. 2–3). Our EMG-driven modeling formulation could estimate reference joint stiffness and torque profiles in a robust way, i.e., EMG-driven models calibrated using 1.6 s of data estimated 100 s of joint torques and stiffness from unseen EMGs and ankle angle profiles (Table 1). Model-based joint stiffness estimations were in line with literature. Recent work estimated ankle stiffness during dynamometry experiments where subjects tracked a sinusoidal plantarflexion torque while the dynamometer imposed a sinusoidal ankle rotation (Ludvig et al., 2022). Even though the protocol involved higher torque levels, their lowest torque level (i.e., between 0 and 10 N·m), yielded a joint stiffness of 25 N·m/rad, which matched the stiffness values we obtained at a plantar-flexion torque level of 10 N·m.

The second test showed there were always more EMG-driven model instances, each of them characterized by different model parameters (Figs. 4–5), that yielded a similar torque fitting error than EMG-driven model instances that yielded a similar total torque + stiffness fitting error (Section 3.2). This provides evidence of the possibility of reducing the MTU parameter solution

space and may facilitate the identification of realistic muscle force solutions that would explain multiple mechanical variables simultaneously.

In the third test, joint stiffness profiles estimated from unperturbed conditions underlay similar trends than stiffness profiles derived from perturbed conditions, with a median RMSE of 0.77 N·m/rad and a median r^2 of 0.67 (Section 3.3, Fig. 6). This indicates that our EMG-driven model, once calibrated using reference data, was able to estimate realistic joint stiffness profiles without needing to perturb the joint. However, despite similarity between the perturbed and unperturbed conditions, our EMG-driven model was also able to capture subtle differences, enabling, for the first time, the study of joint stiffness in natural, unperturbed conditions. This represents a viable way for understanding joint stiffness modulation during functional movements, e.g., locomotion, where it is not possible to perturb the joints without affecting the underlying neuromechanical processes involved. Moreover, the ability to decode joint stiffness from EMGs and joint angles, without the need to apply external perturbations, might radically change the way wearable assistive robots are myoelectrically controlled.

Follow up studies should extend our proposed methodology to generalize to functional movements. Future work should integrate short-range stiffness modules that dynamically engage across static and dynamic movements. Future work should systematically investigate what MTU parameters are most sensitive to stiffness (e.g., slopes of the passive force-length curve and the tendon force-strain curve) and enable direct tuning within our proposed calibration method. Previous work explored ankle joint stiffness estimation techniques by combining ultrasonography and system identification during isometric tasks (Jakubowski et al., 2022). Future work will investigate the integration of ultrasonography within our data-driven modelling framework to refine the estimation of MTU states (e.g., activation, length, velocity) and the calibration of parameters at muscle and tendon scales (e.g., tendon slack length) (Dick et al., 2017).

Currently, a limitation of our EMG-driven model's calibration is that it still requires perturbation-based reference joint stiffness profiles for the initial calibration. Nevertheless, the ability of our EMG-driven modeling framework to estimate joint stiffness without perturbing the joints provides a starting point to relax joint-perturbation constraints post-calibration. Moreover, Fig. 2 and Table 1 provide evidence that EMG-driven models (e.g., subjects 1 and 3) could be potentially calibrated in the "Torque only" condition, while matching reference joint stiffness profiles. Future work will investigate how to constrain MTU parameters during a "Torque only" calibration to enable simultaneous estimation of reference joint stiffness and torque, thereby facilitating our EMG-driven modeling framework's full clinical translation.

Conflict of interest statement

The authors declare no known conflicts of interest concerning this publication.

Acknowledgments

This work was financially supported by the European Research Council (ERC) under the European Union's Horizon 2020 research and innovation program as part of the ERC Starting Grant INTERACT (Grant No. 803035) and by Top Technology Twente Connecting Industry program (TKI Top Sector HTSM) and Stryker European Operations Ltd., Ireland.

References

Brent, R.P., 1973. Some efficient algorithms for solving systems of nonlinear equations. SIAM Journal on Numerical Analysis 10, 327–344. doi:https://doi.org/10.1137/0710031.

Cop, C.P., Cavallo, G., van't Veld, R.C., Koopman, B.F., Lataire, J., Schouten, A.C., Sartori, M., 2021. Unifying system identification and biomechanical formulations for the estimation of muscle, tendon and joint stiffness during human movement. Progress in Biomedical Engineering 3, 033002. doi:https://doi.org/10.1088/2516-1091/ac12c4.

Delp, S.L., Anderson, F.C., Arnold, A.S., Loan, P., Habib, A., John, C.T., Guendelman, E., Thelen, D.G., 2007. Opensim: open-source software to create and analyze dynamic simulations of movement. IEEE transactions on biomedical engineering 54, 1940–1950. doi:https://doi.org/10.1109/tbme.2007.901024.

Delp, S.L., Loan, J.P., Hoy, M.G., Zajac, F.E., Topp, E.L., Rosen, J.M., 1990. An interactive graphics-based model of the lower extremity to study orthopaedic surgical procedures. IEEE Transactions on Biomedical engineering 37, 757–767. doi:https://doi.org/10.1109/10.102791.

Dick, T.J., Biewener, A.A., Wakeling, J.M., 2017. Comparison of human gastrocnemius forces predicted by hill-type muscle models and estimated from ultrasound images. Journal of Experimental Biology 220, 1643–1653. doi:https://doi.org/10.1242/jeb.154807.

Durandau, G., Farina, D., Sartori, M., 2017. Robust real-time musculoskeletal modeling driven by electromyograms. IEEE transactions on biomedical engineering 65, 556–564. doi:https://doi.org/10.1109/TBME.2017.2704085.

Esteban, A.M., van 't Veld, R.C., Cop, C.P., Durandau, G., Sartori, M., Schouten, A.C., 2019. Estimation of time-varying ankle joint stiffness under dynamic conditions via system identification techniques, in: 2019 41st Annual International Conference of the IEEE Engineering in Medicine and Biology Society (EMBC), IEEE. pp. 2119–2122. doi:https://doi.org/10.1109/EMBC.2019.8856423.

Falisse, A., Van Rossom, S., Jonkers, I., De Groote, F., 2016. Emg-driven optimal estimation of subject-specific hill model muscle–tendon parameters of the knee joint actuators. IEEE Transactions on Biomedical Engineering 64, 2253–2262. doi:https://doi.org/10.1109/tbme.2016.2630009.

Goffe, W.L., Ferrier, G.D., Rogers, J., 1994. Global optimization of statistical functions with simulated annealing. Journal of econometrics 60, 65–99. doi:https://doi.org/10.1016/0304-4076(94)90038-8.

Hermens, H.J., Freriks, B., Disselhorst-Klug, C., Rau, G., 2000. Development of recommendations for semg sensors and sensor placement procedures. Journal of electromyography and Kinesiology 10, 361–374. doi:https://doi.org/10.1016/S1050-6411(00)00027-4.

Herzog, W., 2017. Skeletal muscle mechanics: questions, problems and possible solutions. Journal of neuroengineering and rehabilitation 14, 98. doi:https://doi.org/10.1186/s12984-017-0310-6.

Hu, X., Murray, W.M., Perreault, E.J., 2011. Muscle short-range stiffness can be used to estimate the endpoint stiffness of the human arm. Journal of neurophysiology 105, 1633–1641. doi:https://doi.org/10.1152/jn.00537.2010.

Jakubowski, K.L., Ludvig, D., Bujnowski, D., Lee, S.S., Perreault, E.J., 2022. Simultaneous quantification of ankle, muscle, and tendon impedance in humans. IEEE Transactions on Biomedical Engineering doi:https://doi.org/10.1109/tbme.2022.3175646.

Jenkins, T., Bryant, M., 2020. Pennate actuators: force, contraction and stiffness. Bioinspiration & Biomimetics 15, 046005. doi:https://doi.org/10.1088/1748-3190/ab860f.

Kearney, R.E., Hunter, I.W., 1990. System identification of human joint dynamics. Critical reviews in biomedical engineering 18, 55–87.

Klomp, A., De Groot, J.H., De Vlugt, E., Meskers, C.G., Arendzen, J.H., Van Der Helm, F.C., 2013. Perturbation amplitude affects linearly estimated neuromechanical wrist joint properties. Ieee Transactions on Biomedical Engineering 61, 1005–1014. doi:https://doi.org/10.1109/TBME.2013.2290022.

Lloyd, D.G., Besier, T.F., 2003. An emg-driven musculoskeletal model to estimate muscle forces and knee joint moments in vivo. Journal of biomechanics 36, 765–776. doi:https://doi.org/10.1016/s0021-9290(03)00010-1.

Ludvig, D., Perreault, E.J., 2012. System identification of physiological systems using short data segments. IEEE Transactions on Biomedical Engineering 59, 3541–3549. doi:10.1109/TBME.2012.2220767.

Ludvig, D., Whitmore, M.W., Perreault, E.J., 2022. Leveraging joint mechanics simplifies the neural control of movement. Frontiers in Integrative Neuroscience 16, 802608. doi:https://doi.org/10.3389/fnint.2022.802608.

Millard, M., Uchida, T., Seth, A., Delp, S.L., 2013. Flexing computational muscle: modeling and simulation of musculotendon dynamics. Journal of biomechanical engineering 135. doi:https://doi.org/10.1115/1.4023390.

Modenese, L., Ceseracciu, E., Reggiani, M., Lloyd, D.G., 2016. Estimation of musculotendon parameters for scaled and subject specific musculoskeletal models using an optimization technique. Journal of biomechanics 49, 141–148. doi:https://doi.org/10.1016/j.jbiomech.2015.11.006.

Perreault, E.J., Heckman, C.J., Sandercock, T.G., 2003. Hill muscle model errors during movement are greatest within the physiologically relevant range of motor unit firing rates. Journal of biomechanics 36, 211–218. doi:https://doi.org/10.1016/s0021-9290(02)00332-9.

Pizzolato, C., Lloyd, D.G., Sartori, M., Ceseracciu, E., Besier, T.F., Fregly, B.J., Reggiani, M., 2015. Ceinms: A toolbox to investigate the influence of different neural control solutions on the prediction of muscle excitation and joint moments during dynamic motor tasks. Journal of biomechanics 48, 3929–3936. doi:https://doi.org/10.1016/j.jbiomech.2015.09.021.

van de Ruit, M., Mugge, W., Cavallo, G., Lataire, J., Ludvig, D., Schouten, A.C., 2021. Quantitative comparison of time-varying system identification methods to describe human joint impedance. Annual Reviews in Control 52, 91–107. doi:https://doi.org/10.1016/j.arcontrol.2021.10.010.

Sartori, M., Maculan, M., Pizzolato, C., Reggiani, M., Farina, D., 2015. Modeling and simulating the neuromuscular mechanisms regulating ankle and knee joint stiffness during human locomotion. Journal of neurophysiology 114, 2509–2527. doi:https://doi.org/10.1152/jn.00989.2014.

Sartori, M., Reggiani, M., van den Bogert, A.J., Lloyd, D.G., 2012. Estimation of musculotendon kinematics in large musculoskeletal models using multidimensional b-splines. Journal of biomechanics 45, 595–601. doi:https://doi.org/10.1016/j.jbiomech.2011.10.040.

Seth, A., Hicks, J.L., Uchida, T.K., Habib, A., Dembia, C.L., Dunne, J.J., Ong, C.F., DeMers, M.S., Rajagopal, A., Millard, M., Hamner, S.R., Arnold, E.M., Yong, J.R., Lakshmikanth, S.K., Sherman, M.A., Ku, J.P., Delp, S.L., 2018. Opensim: Simulating musculoskeletal dynamics and neuromuscular control to study human and animal movement. PLOS Computational Biology 14, 1–20. doi:https://doi.org/10.1371/journal.pcbi.1006223.

Valero-Cuevas, F.J., 2016. Fundamentals of neuromechanics. Springer. doi:https://doi.org/10.1007/978-1-4471-6747-1.

Winter, D.A., 2009. Biomechanics and motor control of human movement. John Wiley & Sons. doi:https://doi.org/10.1002/9780470549148.

Figures

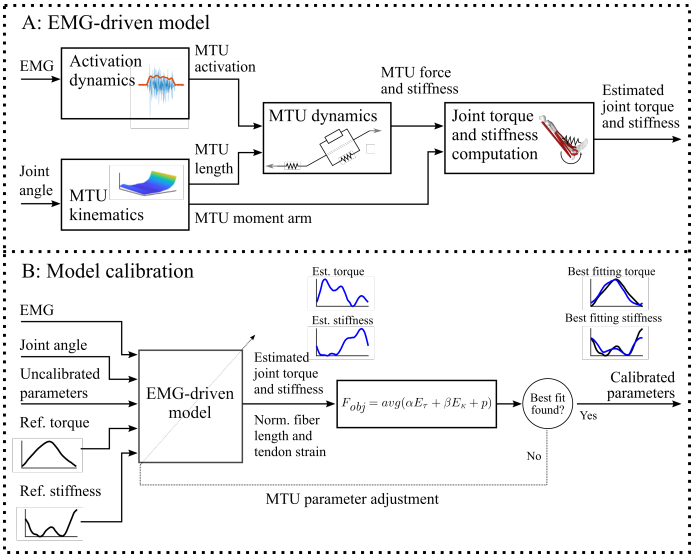

Figure 1: Diagram of the EMG-driven model (A) and the model calibration (B). A) EMG-driven model: the "Activation dynamics" block maps five leg muscle excitations (Section 2.2) into seven muscle-tendon unit (MTU) activations, i.e., the EMG of the peroneus longus muscle was used to drive the modeled peroneus longus and peroneus brevis MTUs, and the EMG of the tibialis anterior was used to drive the modeled peroneus tertius (i.e., a dorsiflexor) MTU. The "MTU kinematics" block maps ankle plantar-dorsi flexion angle into MTU length and moment arms. The "MTU dynamics" block estimates MTU force and stiffness employing a Hill-type muscle model driven by MTU activation and length with an elastic tendon that uses a Wijngaarden–Dekker–Brent optimization (Brent, 1973) to find the roots of the equilibrium equation between muscle fiber force and tendon force. The "Joint torque and stiffness computation" block projects MTU force and stiffness onto the the joint level via the MTU moment arms to obtain estimates of joint torque and stiffness. B) Model calibration: Four parameters per MTU, namely optimal fiber length, tendon slack length, maximum isometric force, and shape factor, are adjusted to best track input reference joint torque and stiffness profiles using the EMG-driven model described in (A). Optimal fiber length and tendon slack length were limited to vary $\pm$ 5 % of their initial value, the maximum isometric force was scaled with a strength coefficient $\in$ (0.3, 2.5) (the MTUs of gastrocnemius lateralis and gastrocnemius medialis, as well as peroneus longus and peroneus brevis, shared the same strength coefficient), and the shape factor could take values $\in$ (-3, 0). A simulated annealing optimization routine is used to adjust MTU parameters until the difference between reference (plots in black) and estimated (plots in blue) joint torque and joint stiffness profiles is minimized. The weights of the contributions of joint torque and stiffness, α and β, respectively, can be tuned to obtain a closer fit to the joint torque or joint stiffness profile.

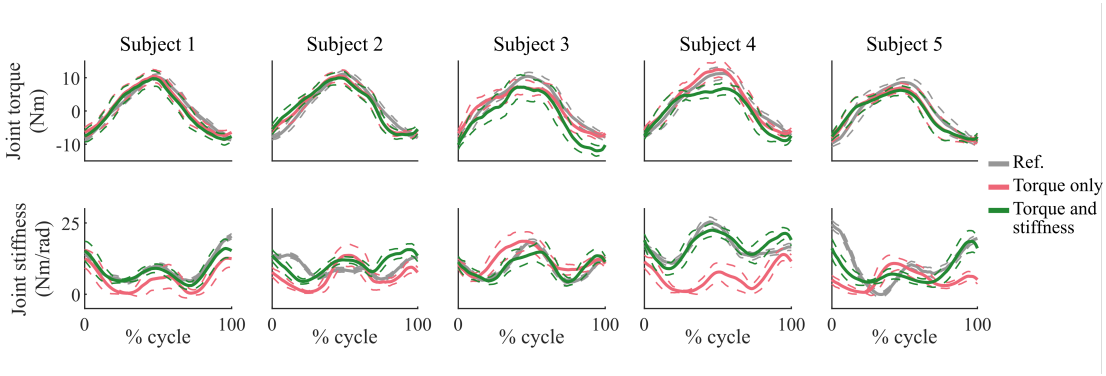

Figure 2: Average joint torque profiles (top row) and joint stiffness profiles (bottom row) for each subject. Reference values, i.e., dynamometer measurements for the joint torque and system identification estimations obtained from perturbation-based data for joint stiffness, are depicted in gray, estimations from the model that was calibrated using the traditional calibration, i.e. $\alpha = 1$ and $\beta = 0$, are depicted in red, and estimations from the model that best fitted reference data, i.e. $\alpha \in [0, 1]$ and $\beta \in [0, 1]$, are depicted in green. Results expressed as mean values (solid line) $\pm$ standard deviation (dashed lines).

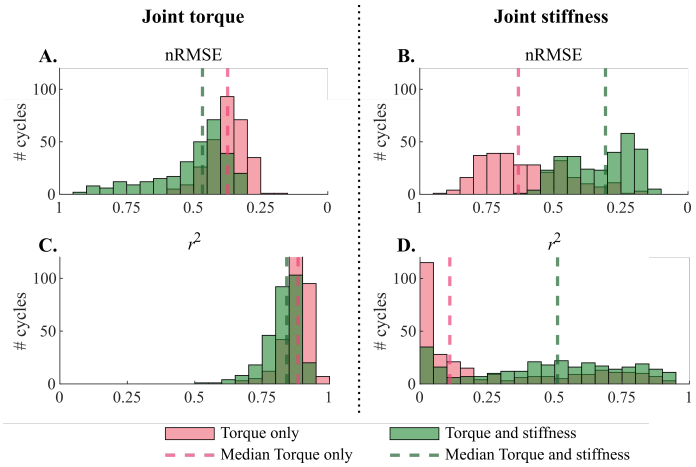

Figure 3: Histograms depicting the distributions, across all cycles of all subjects (n = 297), of normalized root-mean-squared error (nRMSE) values of joint torque (A) and joint stiffness (B) profiles, and squared Pearson correlation coefficient (r^2) values of joint torque (C) and joint stiffness (D) profiles. The dashed vertical lines indicate the median nRMSE and r^2 values. Results of the "Torque only" calibration are shown in red and results of the "Torque and stiffness" calibration are shown in green.

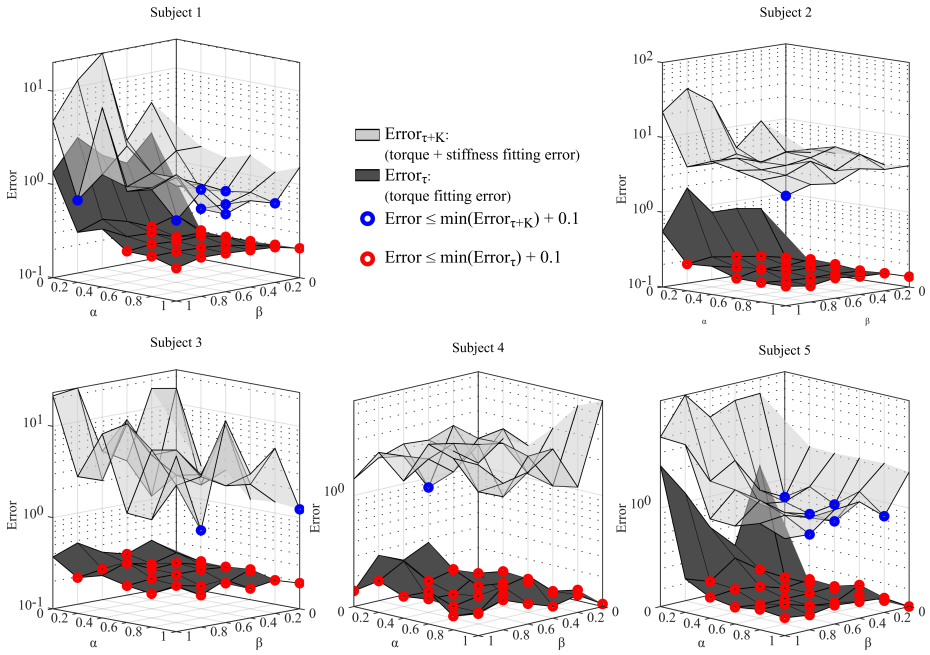

Figure 4: Total torque + stiffness fitting error (light gray) and torque fitting error (dark gray) for each calibrated EMG-driven model using all combinations of α and β for each subject. Red circles indicate the solutions with a torque error $\leq \min(Error_{\tau}) + 0.1$, and blue circles indicate the solutions with a total (i.e. torque + stiffness) error $\leq \min(Error_{\tau+K}) + 0.1$.

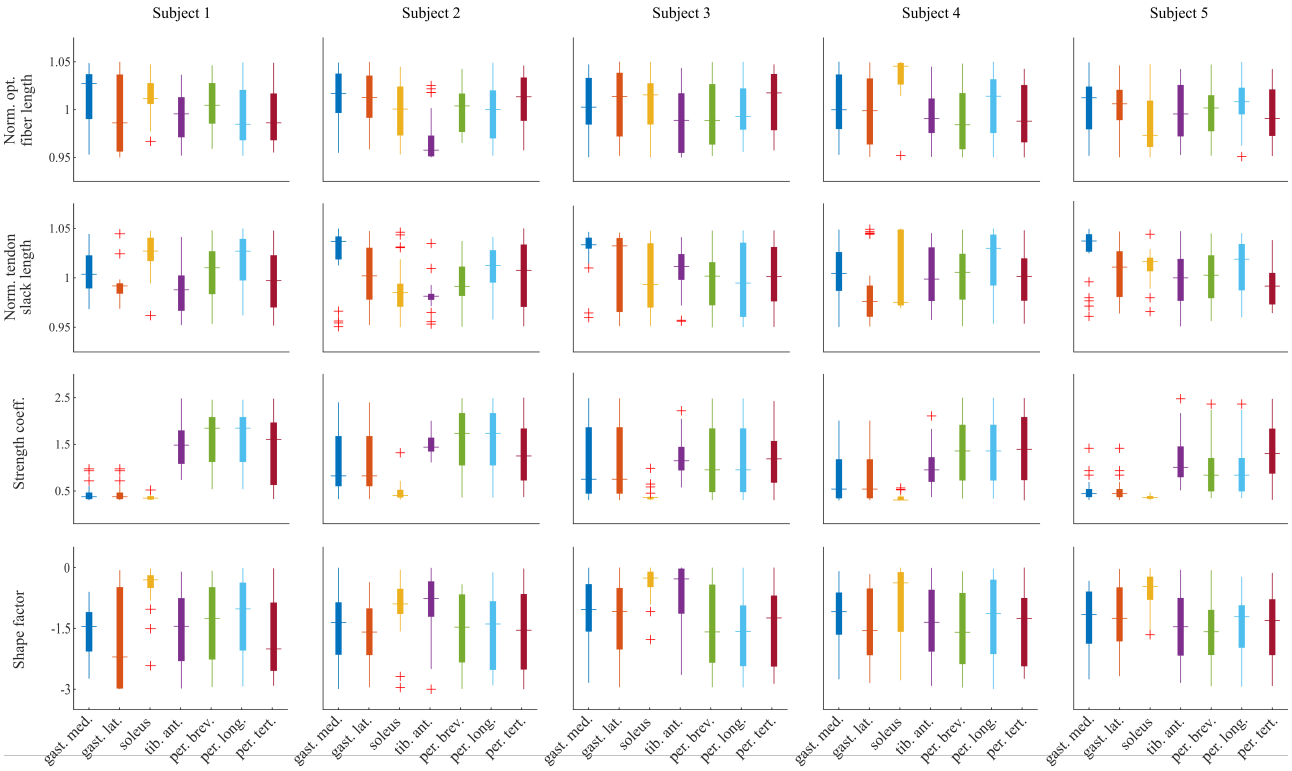

Figure 5: Box plots, for each modelled muscle-tendon unit (MTU) per subject, of the four muscle parameters that are calibrated: optimal fiber length, tendon slack length, strength coefficient, and shape factor. Optimal fiber length and tendon slack length are normalized with their initial uncalibrated value.

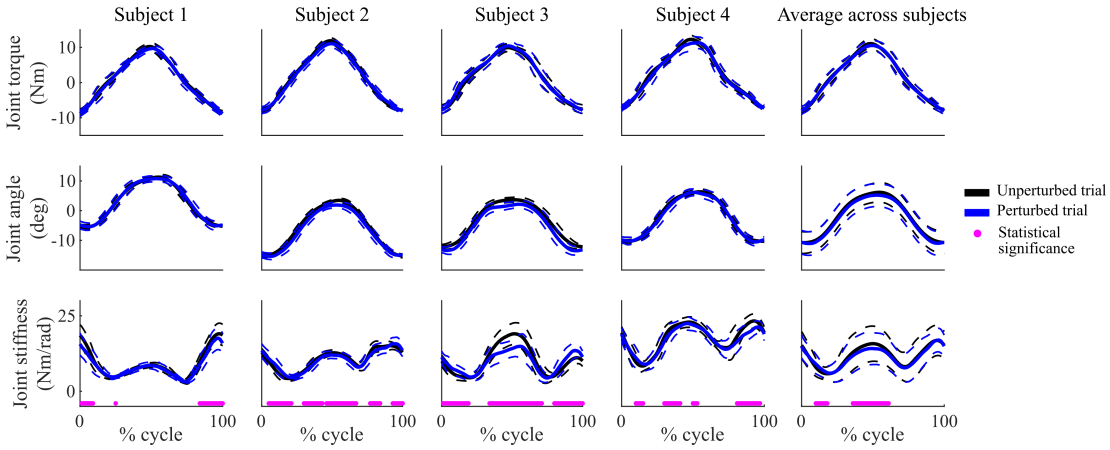

Figure 6: Average joint torque (top row), joint angle (middle row), and joint stiffness profiles (bottom row) for each subject from perturbation-based (blue) and unperturbed (black) data. Magenta dots on the x-axis represent cycle points in which the joint stiffness of the perturbed and the unperturbed condition are different with statistical significance ($p < 0.05$).Results expressed as mean values (solid line) ± standard deviation (dashed lines).